

Article

Impact of Sintering Temperature on the Electrical Properties of $\text{La}_{0.9}\text{Sr}_{0.1}\text{MnO}_3$ Manganite

Wided Hizi ¹, Hedi Rahmouni ¹, Nima E. Gorji ² , Ahlem Guesmi ³, Naoufel Ben Hamadi ³, Lotfi Khezami ³ , Essebti Dhahri ⁴, Kamel Khirouni ⁵ and Malek Gassoumi ^{1,*}

¹ Unité de Recherche Matériaux Avancés et Nanotechnologies (URMAN), Institut Supérieur des Sciences Appliquées et de Technologie de Kasserine, BP 471, Kasserine 1200, Tunisia; widedph@live.com (W.H.); rahmounihedi@yahoo.fr (H.R.)

² School of Engineering, Renewable Energies, Dundalk Institute of Technology, A91 K584 Dundalk, Ireland; nima.s.gorji@gmail.com

³ Department of Chemistry, College of Sciences, Imam Mohammad Ibn Saud Islamic University (IMSIU), P.O. Box 5701, Riyadh 11432, Saudi Arabia; amalkasme@imamu.edu.sa (A.G.); nabenshamadi@imamu.edu.sa (N.B.H.); lhmkhezami@imamu.edu.sa (L.K.)

⁴ Laboratoire de Physique Appliquée, Faculté des Sciences, Université de Sfax, B.P. 1171, Sfax 3000, Tunisia; essebti.dhahri@fss.rnu.tn

⁵ Laboratoire de Physique des Matériaux et des Nanomatériaux Appliquée à l'Environnement, Faculté des Sciences de Gabès Cité Erriadh, Université de Gabès, Gabès 6079, Tunisia; kamelkirouni@yahoo.fr

* Correspondence: malek.gassoumi@fsm.rnu.tn; Tel.: +216-9723-7743



Citation: Hizi, W.; Rahmouni, H.; Gorji, N.E.; Guesmi, A.; Ben Hamadi, N.; Khezami, L.; Dhahri, E.; Khirouni, K.; Gassoumi, M. Impact of Sintering Temperature on the Electrical Properties of $\text{La}_{0.9}\text{Sr}_{0.1}\text{MnO}_3$ Manganite. *Catalysts* **2022**, *12*, 340. <https://doi.org/10.3390/catal12030340>

Academic Editors: Francesco Enrichi, Alberto Vomiero and Elti Cattaruzza

Received: 12 February 2022

Accepted: 8 March 2022

Published: 17 March 2022

Publisher's Note: MDPI stays neutral with regard to jurisdictional claims in published maps and institutional affiliations.



Copyright: © 2022 by the authors. Licensee MDPI, Basel, Switzerland. This article is an open access article distributed under the terms and conditions of the Creative Commons Attribution (CC BY) license (<https://creativecommons.org/licenses/by/4.0/>).

Abstract: $\text{La}_{0.9}\text{Sr}_{0.1}\text{MnO}_3$ nanoparticles were prepared using the citrate–gel route and sintered at different temperatures ($T_S = 600\text{ °C}$, 800 °C , and 1000 °C). The x-ray diffraction patterns reveal that the samples exhibit a single phase with a rhombohedral ($R\bar{3}C$) structure. The transmission electron microscopy technique shows an increase in the grain size when the sintering temperature (T_S) rises. The obtained values are approximately similar to that of crystallite size calculated from x-ray diffraction patterns. The impact of sintering temperature (T_S) on the electrical properties of $\text{La}_{0.9}\text{Sr}_{0.1}\text{MnO}_3$ manganite is examined using the impedance spectroscopy technique. A metal-semiconductor transition at a specific temperature (T_{M-SC}) is observed for all samples. Indeed, the sintering temperature increase induces the shift of this transition temperature toward higher temperatures. Such a behavior is explained by the increase in the grain size. An agreement between the metal-semiconductor transition values coming from the DC resistivity and the grain boundaries analyses is observed. This agreement proves the contribution of the grain boundaries in the electrical properties of the studied samples. In addition, the presence of the relaxation phenomenon is confirmed. The fitted Nyquist plots show the correlation between the microstructure of the material and the electrical properties using an electrical equivalent circuit model. The DC resistivity and the impedance analyses reveal the thermal activation of the transport properties in the investigated system.

Keywords: manganite; sintering temperature; impedance spectroscopy; electrical resistivity

1. Introduction

Manganites constitute one of the most popular families of oxide-perovskites. This popularity comes from its distinguished physical properties. The colossal magnetoresistance effect is pronounced by the close interplay between the magnetic and the electrical transport properties of manganite compounds [1]. In addition, manganites are characterized by phase separation and charge ordering, which make them competitive compounds in magnetic applications, photonic and magnetoelectronic devices, and spintronic technology [2]. The strong correlation between their structural, magnetic, and electrical properties makes these kinds of materials compatible for numerous technological applications [3–9]. Among the manganite systems appropriate for these useful applications, lanthanum manganites ($\text{La}_{1-x}\text{A}_x\text{MnO}_3$) have been extensively studied due to their rich physical properties [10–20].

A focus on their structural properties attests to the fact that they have a general formula— $\text{La}_{1-x}\text{A}_x\text{MnO}_3$ —where La is a rare earth and A is a divalent or monovalent ion. The parent compound LaMnO_3 is known as an anti-ferromagnetic insulator material. Its conductivity is enhanced by the incorporation of the divalent ion Sr^{2+} in LaMnO_3 at the La site. This incorporation produces the proportional converts of Mn^{3+} to Mn^{4+} ion. The formation of the Mn^{4+} ions is generated due to the difference in charge between La^{3+} and Sr^{2+} ions. Indeed, the occurrence of Mn ions is responsible for the double exchange interaction manifested by the whole hops from Mn^{4+} to Mn^{3+} cations [21,22]. These hops are more likely to take place in the ferromagnetic phase where the localized spins of these ions are parallel [21]. This later synchronization between the ferromagnetic behavior and the enhancement of the double exchange mechanism gives an explanation to the metallic ferromagnetic character below the metal-semiconductor transition temperature [23]. Furthermore, the bond angle Mn–O–Mn and bond length Mn–O have a strong dependence on the grain size in manganites [24–28]. So, the electrical information associated with the effects of grains and grain boundaries makes it very important to understand the overall properties of polycrystalline materials. Indeed, the charge carriers transport in these materials can occur by the contribution of grains, the grain boundary, and the sample–electrode interface. By means of the impedance spectroscopy technique, we have the ability to clarify these effects independently [29–34].

Lanthanum–strontium manganites (LSM) currently remain as commonly exploited compounds. Thus, they are used in solid oxide fuel cells as cathode materials due to their mixed conduction properties [35–37]. Vuk Uskokovic et al. [38] have explored their implication in biomedicine by benefiting from their use in hyperthermia treatment. In fact, the use of this compound allowed us the ability to distinguish malignant cells from healthy ones, which are less vulnerable to the increase in temperature. As a consequence, our studied compounds may be exploited in cancer cure [38,39]. Furthermore, given their good catalytic activity and high stability, LSM are used as electro-catalysts. They exhibit electro-conductivity, which is combined to the ionic conductivity provided by the ionic conductor backbones to form high functional cathodes [40]. LSM systems attract the attention of numerous research groups as they undergo a series of structural, electronic, and magnetic phase transitions when they are exposed to variable temperature [1]. Taking into consideration these tremendous usefulness and special properties, LSM were widely studied theoretically [41,42] and experimentally [30–32,43–52] from all sides (i.e., morphologically, structurally, magnetically, and electrically) and in different forms (i.e., bulk, as nanoparticles and thin films [53,54]). The effect of several factors was investigated such as vacancies at the La site [55] and the Mn site [56] as well as oxygen stoichiometry [38,57,58]. In addition, the effect of different amounts of Sr has been explored [59,60]. Old and recent studies have been discussed the effect of introducing an amount of 10% of Sr in an LaMnO_3 system [37,45–49,59]. This interest about the $\text{La}_{0.9}\text{Sr}_{0.1}\text{MnO}_3$ compound is due to its distinctive physical properties. In fact, such a compound is frequently used in solid oxide fuel cells (SOFC) as the cathode. For that reason, the interaction between the $\text{La}_{0.9}\text{Sr}_{0.1}\text{MnO}_3$ cathode and metallic interconnect for a solid oxide fuel cell at reduced temperature has been investigated [37]. In order to more understand the physical properties of this system, Shinde et al. [49] have reported the influence of the annealing temperature on its morphological and magnetic properties. Furthermore, the preparation route determines the electrical and magnetic behavior of LSM. Among the preparation route conditions, the circumstances of the heat treatment (the sintering temperature [1,49,61–66], the sintering time [67,68], the steps followed in sintering, microwave sintering [69,70], the fully or partially annealing [71]) affect the response of lanthanum manganite systems. In fact, the increase in the sintering temperature (T_s) induces a decrease in the electrical resistivity, which leads to the improving of the electrical transport in these materials [62]. Such a result seems to be explained by the increase of the mobility of charge carriers with the increase in T_s . Moreover, the rise in this temperature (T_s) conferred a modification on the metal-semiconductor transition. Several researchers of manganites have reported the

possibility of the shift of this transition temperature (T_{M-SC}) toward the lower [66] and the higher [25,65,66] temperatures with the rise of T_S . The effects of sintering temperature on the physical properties of manganites have been recently reported [72,73]. Accordingly, it is found that T_S affects the grain size, leading to a variation in the metal–insulator transition temperature [72]. Dey and Nath [72] confirm that the grain size variation does not affect the ferromagnetic–paramagnetic transition temperature. In some cases, this thermal excitation causes the disappearance of the transition temperature [26]. Whereas Baaziz et al. [61] found that the metal-semiconductor transition temperature was not affected and estimated it at 160 K for all the sintered samples. In the literature, a complete study on the $La_{0.67}Sr_{0.33}MnO_3$ compound has been investigated [61,74–76]. They started to explore the effect of sintering temperature on the structural and magnetic properties of $La_{0.9}Sr_{0.1}MnO_3$ brought by the variation of particle size [77–79]. In terms of variation as a function of particle size, the evolution of the magnetic properties has been explained by the core–shell model [77]. In addition, the decrease in the Curie temperature (T_C) with the increase in the grain size has been justified by the strain effect of grains induced by the distortion at grain boundaries. In addition, the RCP (Relative Cooling Power) values at a low field are comparable with those of the commercial magnetic refrigerant materials. Such comparison indicates that our compound can act as a candidate for magnetic refrigeration [79]. In the aim of completing the enlightenment of the remaining sides of the whole study, we opt to advance a study on the effect of sintering temperature on the electrical properties of the $La_{0.9}Sr_{0.1}MnO_3$ system.

2. Experimental Details

$La_{0.9}Sr_{0.1}MnO_3$ material was synthesized by the Citrate–Gel route. The nitrate precursors are $La(NO_3)_3 \cdot 6H_2O$, $Mn(NO_3)_2 \cdot 4H_2O$, and $Sr(NO_3)_2$. The stoichiometric amounts of the precursors are dissolved beforehand in water. Then, they are mixed with ethylene glycol ($C_2H_6O_2$) and citric acid ($C_6H_8O_7$), forming a stable solution. The metal/citric acid molar ratio was 1:1. Then, the solution was heated on a thermal plate under constant sintering at 80 °C to remove excess water and obtain a viscous gel. The gel was dried at 130 °C and then calcinated at 600 °C for 12 h. Eventually, the obtained powder is divided into three portions. The first one is the sample sintered at 600 °C. The second and the third portions are sintered at 800 and 1000 °C respectively for 12 h. The phase purity and the structure of the prepared samples were checked by x-ray diffraction (XRD) using the $Cu-K\alpha_1$ radiation source (D5000 diffractometer, BRUKER). The recording of the x-ray powder diagrams was carried out at room temperature in an angular range varying from 10 to 100° with a recording time of 10 s by a step of 0.02°. Transmission electron microscopy (TEM) is used to determine the samples' morphology. Then, the samples are pressed into pellets using a hydraulic press by applying a pressure of 4000 Psi. By means of impedance spectroscopy, the sintered samples were electrically characterized by the following steps. First, thin silver films of some nanometers were deposited on the two opposite faces of the pellets to serve as electrodes. Then, the samples were branched in a Janis VPF 800-cryostat to pick out the electrical measurements using an impedance analyzer 4294A whose frequency range varies from 40 Hz to 10 MHz. We performed the measurements in parallel mode for the equivalent circuit and with an amplitude of 20 mV for the signal. Furthermore, the electrical parameters were recorded in darkness and along the range of temperature extended from 80 to 400 K, using the liquid nitrogen to reach such low temperatures.

3. Results and Discussion

3.1. Structural and Morphological Study

Figure 1a–c show the XRD diagrams of the studied material $La_{0.9}Sr_{0.1}MnO_3$ sintered at 600 (a), 800 (b), and 1000 °C (c). The diagrams present a typical Rietveld refinement including the observed and the calculated data as well as the difference profile. The formation of the perovskite phase $La_{0.9}Sr_{0.1}MnO_3$ is confirmed. The prepared samples were found to be single phase without any detectable impurity, which are crystallized in

the rhombohedral symmetry with the $R\bar{3}c$ space group. The refined lattice parameters are summarized in Table 1.

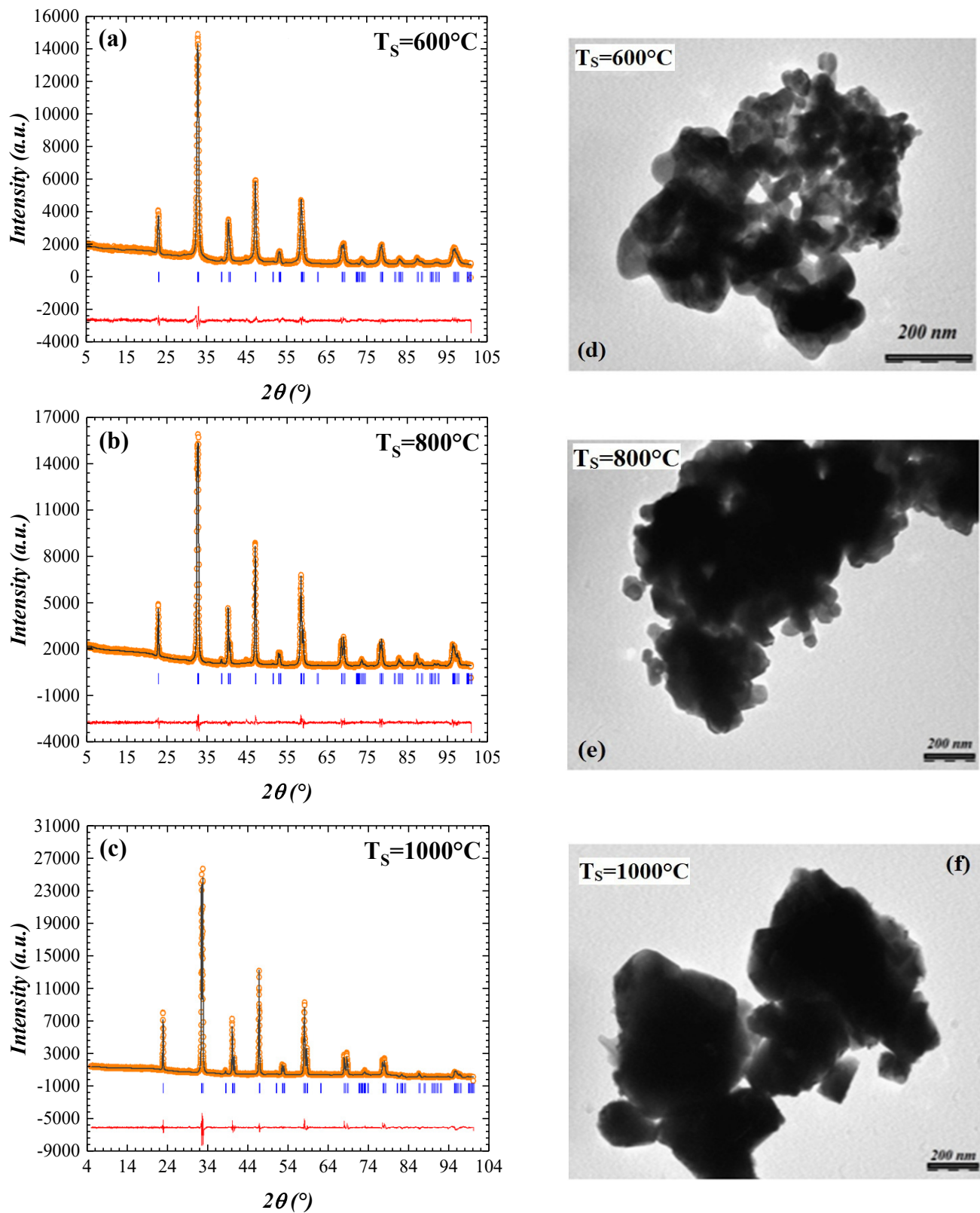


Figure 1. X-ray diffraction patterns and Rietveld refinement of the $\text{La}_{0.9}\text{Sr}_{0.1}\text{MnO}_3$ system sintered at 600 (a), 800 (b), and 1000 °C (c). TEM micrographs of the sintered samples ($T_S = 600^\circ\text{C}$ (d), 800 °C (e), and 1000 °C (f)) for the $\text{La}_{0.9}\text{Sr}_{0.1}\text{MnO}_3$ system.

Table 1. Structural parameters of the $\text{La}_{0.9}\text{Sr}_{0.1}\text{MnO}_3$ system sintered at 600, 800, and 1000 °C.

T_S (°C)	600	800	1000
a(Å)	5.50 ₍₃₎	5.51 ₍₁₎	5.51 ₍₈₎
c(Å)	13.35 ₍₀₎	13.34 ₍₆₎	13.34 ₍₇₎
v(Å ³)	350.14 ₍₇₎	351.11 ₍₄₎	351.92 ₍₈₎
d(XRD) (nm)	45	75	85
d(TEM) (nm)	43	72	84

The unit cell volumes are 350.14₍₇₎, 351.11₍₄₎, and 351.92₍₈₎ Å³ for $T_S = 600, 800,$ and 1000 °C, respectively. For each sample, the average crystallite size was determined based on the full width at half maximum (FWHM) of the Bragg peaks (the intense peaks) and the peak position using the Debye–Scherrer expression as follows:

$$D_{\text{SC}} = \frac{0.9\lambda}{\beta \cos \theta} \quad (1)$$

where β is the full width at half maximum of the Bragg peak, λ is the wavelength of $\text{CuK}\alpha_1$ ($\lambda = 1.5406\text{Å}$), and θ is the diffraction angle of the most intense peak. Table 1 shows the sensibility of the crystallite size ($d(\text{XRD})$) on the sintering process. Indeed, $d(\text{XRD})$ increases with the sintering temperature rise ($d(\text{XRD}) = 45, 75,$ and 85 nm, respectively for $T_S = 600, 800,$ and 1000 °C). Such a result is in good agreement with comparable systems [61]. The increase in the unit cell volume may be due to a strong correlation between the lattice parameters and the grain size. Figure 1d–f shows the representative TEM micrographs for the particles of our samples. The micrographs reveal a variable grain size as a function of the sintering temperature. It exhibits an increase in the grain size ($d(\text{TEM})$) from 43 to 72 to 84 nm with the increase in T_S (Table 1). The calculated crystallite size is practically similar to the grain size. This indicates that each grain is composed by a single crystallite. Figure 1d–f shows also that these nanoparticles combine in agglomerates. As the sintering temperature rises, the agglomeration rate increases. In addition, it is observed that the prepared nanoparticles, with a form that is not completely spherical, have an inhomogeneous size.

3.2. DC-Resistivity Analysis

Figure 2a–c show the temperature dependence of the electrical DC resistivity (ρ_{DC}) for the three studied samples sintered at 600 (a), 800 (b), and 1000 °C (c). There is a similarity in each curve. Then, a metal-semi-conductor transition at $T_{\text{M-SC}}$ was observed. For $T > T_{\text{M-SC}}$, the decrease in ρ_{DC} can be related to the fact that as the temperature rises, more charge carriers are released from the trapped centers and participate in the conduction. In perovskite systems (for $T > T_{\text{M-SC}}$), the electrical conductivity is usually generated by hopping conduction processes [80,81]. The activation of such processes induces the observed resistivity decrease. The inferred values of $T_{\text{M-SC}}$ are depicted in Figure 2d. It can be seen that $T_{\text{M-SC}}$ increases with the increase in T_S , as shown in Figure 2d. Such behavior has been also detected by the increase in the annealing time reported by Banerjee et al. [82] for the $\text{La}_{0.5}\text{Pb}_{0.5}\text{MnO}_3$ compound. For the $\text{La}_{0.67}\text{Sr}_{0.33}\text{MnO}_3$ system, $T_{\text{M-SC}}$ was found by Baaziz et al. [61] to be unaffected by the sintering temperature excitation. For the same system reported by Venkataiah et al. [83], $T_{\text{M-SC}}$ increases from 200 to 270 K with the rise in T_S . Such a difference in results for the same investigated compound ($\text{La}_{0.67}\text{Sr}_{0.33}\text{MnO}_3$) is probably due to the sintering and the synthesis conditions.

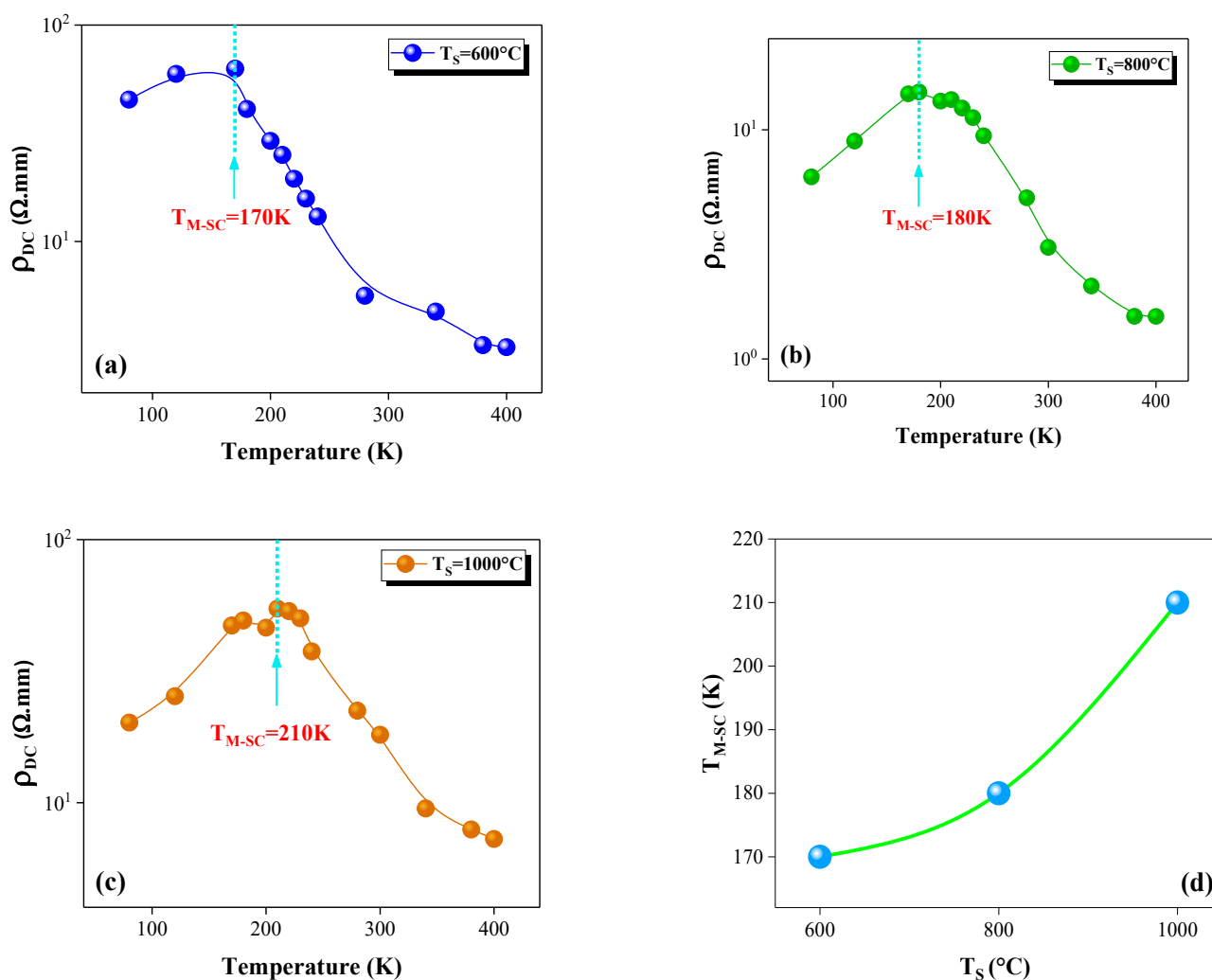


Figure 2. Temperature dependence of the electrical DC-resistivity for the $\text{La}_{0.9}\text{Sr}_{0.1}\text{MnO}_3$ compound at different sintering temperatures ($T_S = 600^\circ\text{C}$ (a), 800°C (b), and 1000°C (c)). Evolution of T_{M-SC} with sintering temperature T_S (d).

The metal-semiconductor transition temperature can be explained by the DE mechanism, which can be affected by the grain boundary region. In fact, T_{M-SC} may be correlated to a variation made on the stoichiometric ratio of $\text{Mn}^{3+}/\text{Mn}^{4+}$, the bond angle Mn-O-Mn ($\theta_{\text{Mn-O-Mn}}$), or the bond length Mn-O ($d_{\text{Mn-O}}$). In the present thermal excitation, the shift of T_{M-SC} toward higher temperatures can be attributed to the reduction of the double exchange interactions as T_S rises. This reduction may be a result of an increase in $\theta_{\text{Mn-O-Mn}}$ or $d_{\text{Mn-O}}$ caused by the detected increase in the unit cell volume (Table 1) as a function of particle size [24–27] or the fact that parts of the $\text{Mn}^{3+}-\text{O}^{2-}-\text{Mn}^{4+}$ network are broken. The representative TEM (transmission electron microscopy) micrographs (Figure 1d–f) exhibit an increase in the grain size from 43 to 72 to 84 nm with the increase in T_S (Table 1). Such an increase indicates that the particle size might have a considerable influence on these previously mentioned parameters, leading to its role in the shift of T_{M-SC} . In a microstructure view of the samples, manganites are composed of two regions: a ferromagnetic-metallic one linked with the paramagnetic-insulating region. In addition, it is known that the electrical resistivity is strongly influenced by the region of the grain boundaries. This region can behave as an improved scattering center for the conductive electron. Consequently, the increase in grain size causes a reduction in the number of grain boundaries, leading to the decrease in this insulating region as well as the enhancement of the grain connectivity. The ascending of T_{M-SC} values is expected [25,27,82,83]. An agreement with the

literature [25,27,63–65,82–85] for comparable cases in manganites was confirmed. For the $\text{La}_{0.85}\text{K}_{0.15}\text{MnO}_3$ compound [65], this heat treatment results an increase in the crystallite size (from 31.5 to 78.8 nm) as well as the grain size (from 85 to 490 nm). In addition, as T_S rises, the unit cell volume increase leads to the detected increase $\text{ind}_{\text{Mn-O}}$ with a constant value of $\theta_{\text{Mn-O-Mn}}$. These factors cause the mentioned shift of $T_{\text{M-SC}}$ toward room temperature (from 281 to 290K) [65].

3.3. Impedance Analysis

The spectra of the normalized imaginary part of the impedance Z'' (Figure 3a–c) are characterized by the appearance of a peak at a specific frequency (f_r) for each temperature curve.

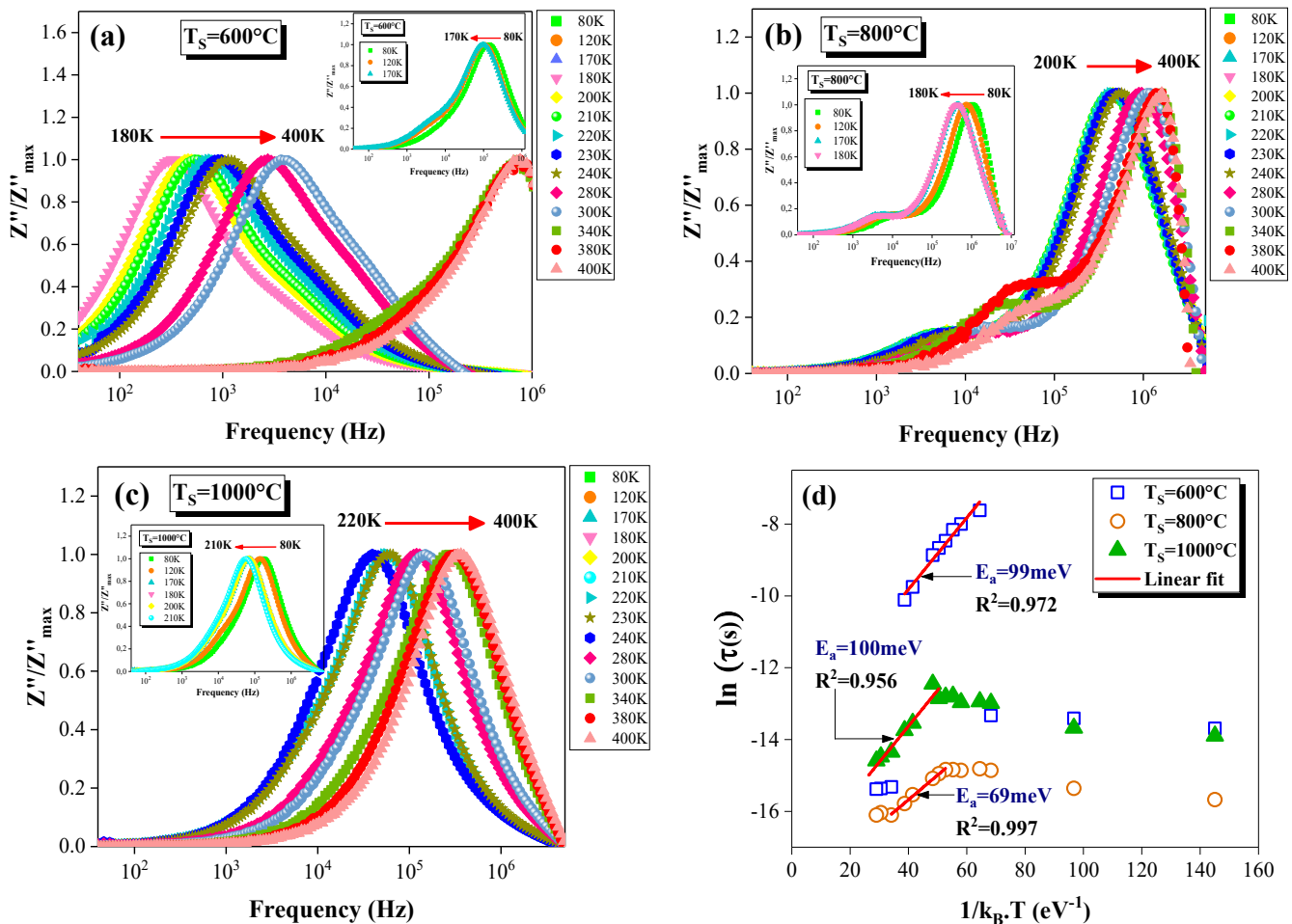


Figure 3. Frequency dependence of the normalized imaginary part of the impedance (Z'') at different temperatures for $\text{La}_{0.9}\text{Sr}_{0.1}\text{MnO}_3$ compound sintered at 600°C (a), 800°C (b), and 1000°C (c). Plot of $\ln(\tau)$ versus the inverse of temperature ($1/k_B \times T$) of the $\text{La}_{0.9}\text{Sr}_{0.1}\text{MnO}_3$ compound at different sintering temperatures (d).

This specific frequency is known as “the relaxation frequency”. The displacement of f_r , the center of each peak, with temperature allows visualizing clearly the imprints of the metal-semiconductor transition. Such behavior has been also observed for the $\text{La}_{0.6}\text{Sr}_{0.2}\text{Na}_{0.2}\text{MnO}_3$ compound [14]. Below $T_{\text{M-SC}}$ for each sample, the peak shifts toward low frequencies, as depicted in the inset of Figure 3a–c. Such an observation constitutes a good concretization of the metallic behavior. Above $T_{\text{M-SC}}$, an opposite displacement takes place, reflecting a semiconductor behavior proved by a thermally activated process (Figure 3a–c). Accordingly, the shift of this peak as a function of the temperature indicates the presence of the relaxation phenomenon in the investigated compound. Several groups

of researchers have observed the contribution of this phenomenon in the conduction for different perovskite-type manganites [29–32,86]. However, the presence of this relaxation phenomenon is correlated to the presence of electrons/immobile species at low temperatures and defects/vacancies at the higher temperature side [86]. At lower frequencies, a second relaxation peak with a lower peak magnitude than the previous one is observed. Such an observation reveals the presence of two relaxation processes, which is clearly shown for the sample sintered at 800 °C. Numerous studies have found this experimental result in manganites [87–89]. Indeed, for the BaMnO₃ manganite compound [88], the appearance of this second peak at low frequencies is confirmed. Accordingly, the relaxation frequency f_r and its corresponding relaxation time τ values are deduced from each peak using the following relation:

$$2\pi f_r \cdot \tau = 1 \quad (2)$$

As shown in Figure 3d, the relaxation time $\ln(\tau)$ varies linearly against the inverse of temperature ($1/k_B \cdot T$). Such a variation confirms that it obeys the Arrhenius law [90]:

$$\tau(T) = \tau_0 \exp(-E_a/(k_B \cdot T)) \quad (3)$$

where τ_0 is constant. The activation energy (E_a) values deduced from the slopes of these linear variations are shown in Figure 3d.

Figure 4a–c present the Nyquist diagrams of the studied samples. The diagrams are characterized by the presence of two overlapped semi-circle arcs with a conserved shape when the temperature increases. The overlapped nature of these arcs corresponds to the existence of more than one relaxation phenomenon, in which they are associated to different electro-active regions [91]. The overlap degree of the two arcs suggests that the relaxation frequencies of each contribution are very close. The evolution of the diameter of these arcs with the temperature excitation is another manifestation of the metal-semiconductor transition. Indeed, for the observed semi-conductor behavior, the diameter of the semi-circle decreases as the temperature rises (Figure 4a–c). The insets of Figure 4 (a–c) show an increase in this diameter with temperature. Such behavior confirms the metallic character. So, the T_{M-SC} values are detected at 170 K, 180 K, and 210 K for $T_S = 600, 800,$ and 1000 °C, respectively. Such values confirm the strong agreement between the impedance results and the resistivity evolution.

In order to examine the participation of the grains and grain boundaries regions as well as the electrodes in the electrical conduction, we have modeled the investigated samples to an electrical equivalent circuit. $[R_g + (R_{gb} // CPE_{gb}) + (R_e // CPE_e)]$ is the most appropriate equivalent circuit, which is plotted in the insets of Figure 4a–c (where $R_g, R_{gb},$ and R_e are the grain, grain boundary, and electrodes resistances, respectively, and CPE_{gb} and CPE_e are the constant phase elements of the grain boundary and electrodes, respectively). Such a model allowed us to correlate between the electrical properties and the microstructure of this material. As shown in Figure 4a–c, the obtained experimental data were well fitted using Z-view software. According to this model, the first semi-circle presents the contribution of grains and grain boundaries [88,89], and the second one at low frequencies can be associated to the electrodes effect [88,89]. Moreover, the impedance response of grains dominates at high frequencies. Indeed, the left intercept of the first cited semi-circle with the real impedance axis is attributed to the grain resistance. The diameter of this semi-circle provides the grain boundary resistance. Accordingly, the right intercept at low frequencies is ascribed to the total resistance of the samples $R_T = R_g + R_{gb} + R_e$. The fitted values of these resistances are shown in Table 2.

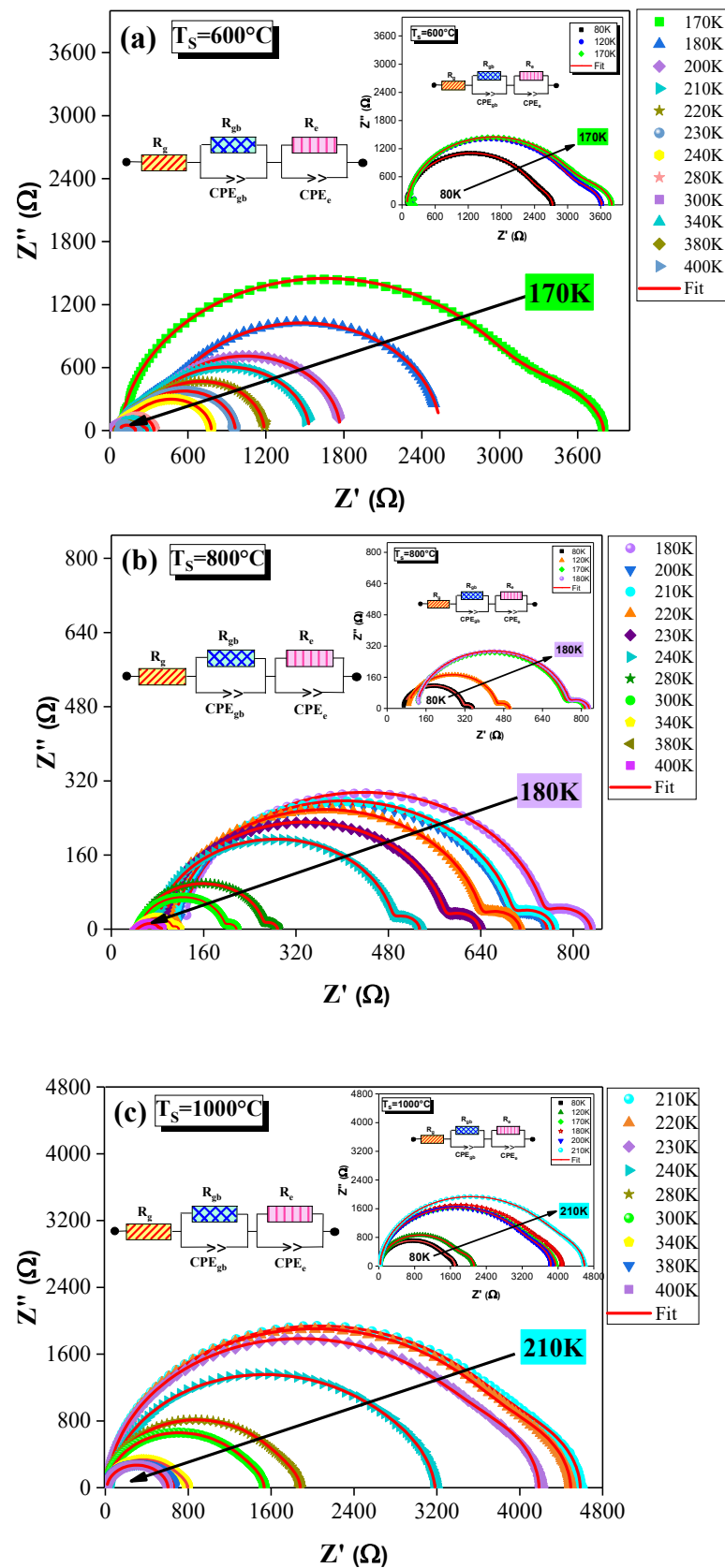


Figure 4. The Nyquist diagrams of $\text{La}_{0.9}\text{Sr}_{0.1}\text{MnO}_3$ system sintered at 600°C (a), 800°C (b), and 1000°C (c).

Table 2. Fitted values of grains, grain boundaries, and electrodes resistances extracted from the electrical equivalent circuit model.

T _S (°C)		600			800			1000		
		Resistance (Ω)								
T (K)	R _g	R _{gb}	R _e	R _g	R _{gb}	R _e	R _g	R _{gb}	R _e	
80	63	2390	272	68	248	35	4	1551	150	
120	80	3065	473	85	370	49	22	1800	300	
170	80	3150	570	120	617	77	29	3450	460	
180	125	300	2120	121	633	77	29	3587	470	
200	105	215	1455	110	582	63	27	3415	400	
210	88	180	1268	108	592	66	22	4057	505	
220	74	150	964	95	550	63	23	3985	489	
230	65	120	780	90	492	56	21	3685	480	
240	63	102	616	79	412	43	23	3000	160	
280	37	45	257	52	214	22	13	1717	151	
300	29	30	180	50	148	19	13	1390	130	
340	65	207	16	19	87	11	12	697	84	
380	70	122	6	19	61	6	13	590	55	
400	70	123	4	17	65	5	14	568	22	

Table 2 shows the reduction of electrode response with the rise of temperature for different T_S. Such evolution may be related to the fact that the charge carriers' mobility increases at the sample–electrode interface as the temperature rises. For the sample sintered at 600 °C, the electrodes region is much more resistive than the grain boundary (R_e >> R_{gb}), as the sample starts to behave as a semi-conductor (T > T_{M-SC}). Therefore, the electrodes response is responsible for the reduction of the grain boundary effect. So, in this temperature range, the contribution of the electrodes region in the conduction process is more important than the grain boundaries. Then, as the temperature rises, the grain boundary returns to be more resistive than the electrodes region for 340 K–400 K. As T_S rises from 600, 800, or 1000 °C (and grain size increases), this observation is suppressed, and the grain boundaries recover their higher resistance values (Table 2). As it can be seen for the sample sintered at 800 °C, the electrodes resistance is lower than the grains and the grain boundary ones (R_e < R_g < R_{gb}). As the sintering temperature increases from 800 to 1000 °C, accordingly, the grain size increases, and the electrodes resistance becomes higher than the grain one (R_g < R_e < R_{gb}). Furthermore, R_g values are very low compared to R_{gb} (R_g << R_{gb}) [13,29–32]. In manganites, the grain boundaries are more resistive than the grains [13,29–32,91]. Such a result can be related to the existence of different conventional electro-active phases [91].

The grain boundary plays a decisive role in the determination of transport properties in manganite oxides [13–15,29–32]. Its resistance variation with temperature is represented in Figure 5a. Indeed, R_{gb} increases, sculpting the traces of a metallic behavior. Then, it decreases following a thermally activated process in a semi-conductor behavior. This decrease can be related to the fact that the grain boundaries effect has assisted in the reduction of the barrier against the charge carriers hopping. Thereby, it has paved the way to enhance the electrical transport with the temperature increase [30,32]. Hence, the previous T_{M-SC} evolution is confirmed (Figure 5b). The evolution already discussed R_{gb} values with temperature for the sample sintered at 600 °C, which is represented in Figure 5a. This evolution is also observed in Figure 5c, which depicts the plot of the resistivity against temperature for different frequencies.

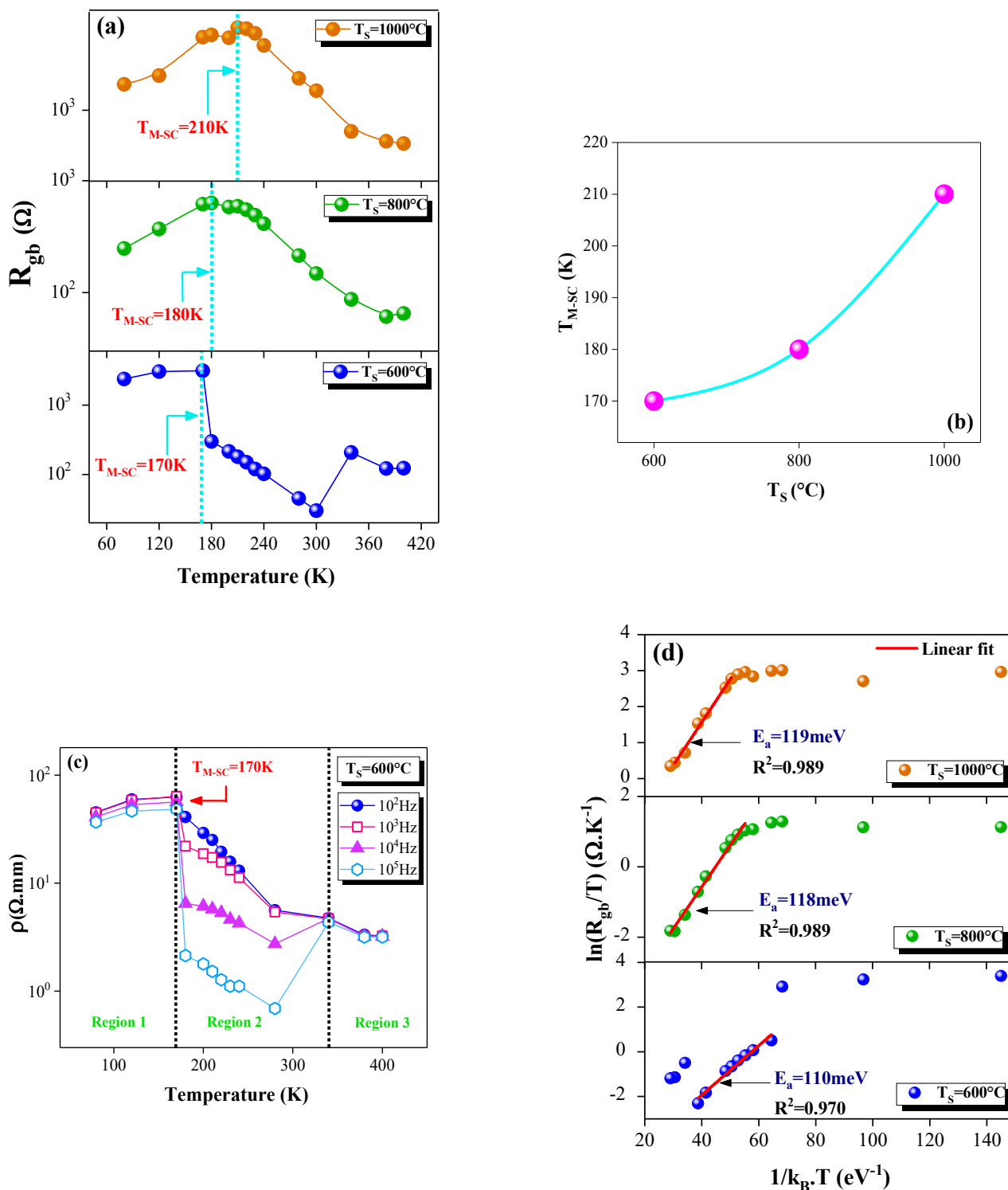


Figure 5. Temperature dependence of the grain boundary resistance for the $\text{La}_{0.9}\text{Sr}_{0.1}\text{MnO}_3$ compound at different sintering temperatures (a). Evolution of T_{M-SC} with sintering temperature T_s (b). Temperature dependence of the electrical resistivity for the sample sintered at 600°C performed at different frequencies (c). Plot of $\ln(R_{gb}/T)$ against $(1/k_B \times T)$ at different sintering temperatures (d).

In the temperature range of 80–170 K (region 1), the resistivity is practically frequency independent in which the curves are combined. Then, as the temperature rises in region 2, the resistivity is strongly dependent on frequency. Indeed, a significant decrease in the electrical resistivity is observed. Such a result may be due to the pumping force of

the applied frequency that excites the trapped centers of charge carriers for the gradual evacuation when the frequency increases [92]. In turn, this causes the participation of more charge carriers in the conduction process and therefore the improving of transport properties. Such a variation confirms the evolution mentioned above of the R_{gb} values, which are also obtained at high frequencies (Figure 5a). This similarity in their behaviors proves the contribution of the grain boundary region in conduction. In region 3, the resistivity is frequency independent, which can be employed in suitable applications. Figure 5d depicted the plots of $\ln(R_{gb}/T)$ against $(1/k_B \cdot T)$. The curves are well fitted by a straight line for $T > T_{M-SC}$. From this linear variation, we deduce the activation energy value for each sintered sample. In fact, in manganites, the electrical transport properties are governed by the grain boundary region effects [13,15].

4. Conclusions

In this study, the effects of sintering temperature on the electrical properties of the $\text{La}_{0.9}\text{Sr}_{0.1}\text{MnO}_3$ compound are explored. The citrate–gel method is used to prepare the studied samples. The XRD study shows the samples crystallization in the rhombohedral symmetry with the space group. The XRD and TEM analyses prove the increase in the crystallite and grain size under the sintering temperature effect. A metal–semi-conductor transition is observed for all samples, whereas the metallic character extends over a longer temperature range as T_S rises. Such a shift of T_{M-SC} toward high temperatures seems to be assigned to structural and morphological changes, and it is comparable to that reported in the literature. The impedance analysis confirms the existence of the electrical relaxation phenomenon. $[R_g + (R_{gb} // CPE_{gb}) + (R_e // CPE_e)]$ is the most suitable equivalent circuit model to describe our material. The resemblance in the resistivity and the grain boundaries variations with temperature confirms the contribution of the grain boundaries in the electrical transport properties.

Author Contributions: W.H., paper writing; H.R., data manipulation; M.G., data manipulation; A.G., data manipulation; N.B.H., paper editing and English correction; L.K., English correction E.D., paper editing and English correction; K.K., data manipulation. N.E.G. contributed in conceptualization, experiments, manuscript review. All authors have read and agreed to the published version of the manuscript.

Funding: Deanship of Scientific Research at Imam Mohammad Ibn Saud Islamic University.

Data Availability Statement: Not applicable.

Acknowledgments: The authors extend their appreciation to the Deanship of Scientific Research at Imam Mohammad Ibn Saud Islamic University for funding this work through Re-search Group no. RG-21-09-67.

Conflicts of Interest: The authors declare no conflict of interest.

References

1. Dutta, A.; Gayathri, N.; Ranganathan, R. Effect of particle size on the magnetic and transport properties of $\text{La}_{0.875}\text{Sr}_{0.125}\text{MnO}_3$. *Phys. Rev. B* **2003**, *68*, 054432. [[CrossRef](#)]
2. Jin, S.; Tifel, T.H.; Cormack, M.M.; Fastenacht, R.A.; Ramesh, R.; Chen, L.H. Thousandfold change in resistivity in magnetoresistive La–Ca–Mn–O films. *Science* **1994**, *264*, 413–415. [[CrossRef](#)]
3. Kolat, V.S.; Gencer, H.; Gunes, M.; Atalay, S. Effect of B-doping on the structural, magnetotransport and magnetocaloric properties of $\text{La}_{0.67}\text{Ca}_{0.33}\text{MnO}_3$ compounds. *Mater. Sci. Eng. B* **2007**, *140*, 212–217. [[CrossRef](#)]
4. Zhang, Q.; Yin, L.; Mi, W.; Wang, X. Large Spatial Spin Polarization at Benzene/ $\text{La}_{2/3}\text{Sr}_{1/3}\text{MnO}_3$ Spinterface: Toward Organic Spintronic Devices. *J. Phys. Chem. C* **2016**, *120*, 6156–6164. [[CrossRef](#)]
5. Yang, Q.; Yao, J.; Zhang, K.; Wang, W.; Zuo, X.; Tang, H.; Wu, M.; Li, G. Perovskite-type $\text{La}_{1-x}\text{Ca}_x\text{MnO}_3$ manganese oxides as effective counter electrodes for dye-sensitized solar cells. *J. Electroanal. Chem.* **2019**, *833*, 1–8. [[CrossRef](#)]
6. Pankhurst, Q.A.; Connolly, J.; Jones, S.K.; Dobson, J. Applications of magnetic nanoparticles in biomedicine. *J. Phys. D Appl. Phys.* **2003**, *36*, R167. [[CrossRef](#)]
7. Zhang, S.; Dong, G.; Liu, Y.; Li, H.; Chu, K.; Pu, X.; Yu, X.; Liu, X. Effect of Na-doping on structural, electrical, and magnetoresistive properties of $\text{La}_{0.7}(\text{Ag}_{0.3-x}\text{Na}_x)_{0.3}\text{MnO}_3$ polycrystalline ceramics. *Ceram. Int.* **2020**, *46*, 584–591. [[CrossRef](#)]

8. Assoudi, N.; Walha, I.; Dhahri, E. Physical properties of double-doping Lanthanum manganite for bolometer applications. *Chem. Phys. Lett.* **2019**, *731*, 136609. [[CrossRef](#)]
9. Patra, A.S.; Kumar, N.V.; Barpuzary, D.; De, M.; Qureshi, M. Strontium doped lanthanum manganites for efficient and robust photocatalytic water oxidation coupled with graphene oxide. *Mater. Lett.* **2014**, *131*, 125–127. [[CrossRef](#)]
10. Rahmouni, H.; Cherif, B.; Baazaoui, M.; Khirouni, K. Effects of iron concentrations on the electrical properties of $\text{La}_{0.67}\text{Ba}_{0.33}\text{Mn}_{1-x}\text{Fe}_x\text{O}_3$. *J. Alloys Compd.* **2013**, *575*, 5–9. [[CrossRef](#)]
11. Rahmouni, H.; Cherif, B.; Jemai, R.; Dhahri, A.; Khirouni, K. Europium substitution for lanthanum in LaBaMnO —The structural and electrical properties of $\text{La}_{0.7-x}\text{Eu}_x\text{Ba}_{0.3}\text{MnO}_3$ perovskite. *J. Alloys Compd.* **2017**, *690*, 890–895. [[CrossRef](#)]
12. Rahmouni, H.; Dhahri, A.; Khirouni, K. The effect of tin addition on the electrical conductivity of Sn-doped LaBaMnO_3 . *J. Alloys Compd.* **2014**, *591*, 259–262. [[CrossRef](#)]
13. Rahmouni, H.; Smari, M.; Cherif, B.; Dhahri, E.; Khirouni, K. Conduction mechanism, impedance spectroscopic investigation and dielectric behavior of $\text{La}_{0.5}\text{Ca}_{0.5-x}\text{Ag}_x\text{MnO}_3$ manganites with compositions below the concentration limit of silver solubility in perovskites ($0 \leq x \leq 0.2$). *Dalton Trans.* **2015**, *44*, 10457. [[CrossRef](#)]
14. Charguia, R.; Hcini, S.; Boudard, M.; Dhahri, A. Microstructural properties, conduction mechanism, dielectric behavior, impedance and electrical modulus of $\text{La}_{0.6}\text{Sr}_{0.2}\text{Na}_{0.2}\text{MnO}_3$ manganite. *J. Mater. Sci. Mater. Electron.* **2019**, *30*, 2975–2984. [[CrossRef](#)]
15. Elghoul, N.; Wali, M.; Kraiem, S.; Rahmouni, H.; Dhahri, E.; Khirouni, K. Sodium deficiency effect on the transport properties of $\text{La}_{0.8}\text{Na}_{0.2-x}\text{MnO}_3$ manganites. *Phys. B Phys. Condens. Matter* **2015**, *478*, 108–112. [[CrossRef](#)]
16. Choura-Maatar, S.; Nofal, M.; M'nassri, R.; Cheikhrouhou-Koubaa, W.; Chniba-Boudjada, N.; Cheikhrouhou, A. Enhancement of the magnetic and magnetocaloric properties by Na substitution for Ca of $\text{La}_{0.8}\text{Ca}_{0.2}\text{MnO}_3$ manganite prepared via the Pechini-type sol–gel process. *J. Mater. Sci. Mater. Electron.* **2020**, *31*, 1634–1645. [[CrossRef](#)]
17. Mahjoub, S.; M'nassri, R.; Baazaoui, M.; Hlil, E.K.; Oumezzine, M. Tuning magnetic and magnetocaloric properties around room temperature via chromium substitution in $\text{La}_{0.65}\text{Nd}_{0.05}\text{Ba}_{0.3}\text{MnO}_3$ system. *J. Magn. Magn. Mater.* **2019**, *481*, 29–38. [[CrossRef](#)]
18. M'nassri, R.; Cheikhrouhou-Koubaa, W.; Boudjada, N.C.; Cheikhrouhou, A. Effect of barium-deficiency on the structural, magnetic, and magnetocaloric properties of $\text{La}_{0.6}\text{Sr}_{0.2}\text{Ba}_{0.2-x}\text{MnO}_3$ ($0 \leq x \leq 0.15$). *J. Appl. Phys.* **2013**, *113*, 073905. [[CrossRef](#)]
19. Baazaoui, M.; Oumezzine, M.; Cheikhrouhou-Koubaa, W. Critical Behavior in Ga-Doped Manganites $\text{La}_{0.65}\text{Bi}_{0.05}\text{Sr}_{0.3}\text{Mn}_{1-x}\text{Ga}_x\text{O}_3$ ($x = 0$ and 0.06). *Phys. Solid State* **2020**, *62*, 278–284. [[CrossRef](#)]
20. Liu, Y.; Sun, T.; Dong, G.; Zhang, S.; Chu, K.; Pu, X.; Li, H.; Liu, X. Dependence on sintering temperature of structure, optical and magnetic properties of $\text{La}_{0.625}\text{Ca}_{0.315}\text{Sr}_{0.06}\text{MnO}_3$ perovskite nanoparticles. *Ceram. Int.* **2019**, *45*, 17467–17475. [[CrossRef](#)]
21. Zener, C. Interaction between the d-Shells in the Transition Metals. II. Ferromagnetic Compounds of Manganese with Perovskite Structure. *Phys. Rev.* **1951**, *82*, 403–405. [[CrossRef](#)]
22. de Gennes, P.G. Effects of Double Exchange in Magnetic Crystals. *Phys. Rev.* **1960**, *118*, 141–154. [[CrossRef](#)]
23. Lakshmi, Y.K.; Venkataiah, G.; Vithal, M.; Reddy, P.V. Magnetic and electrical behavior of $\text{La}_{1-x}\text{A}_x\text{MnO}_3$ (A = Li, Na, K and Rb) manganites. *Phys. B Condens. Matter* **2008**, *403*, 3059–3066. [[CrossRef](#)]
24. Zhang, N.; Yang, W.; Ding, W.; Xing, D.; Du, Y. Grain size-dependent magnetism in fine particle perovskite, $\text{La}_{1-x}\text{Sr}_x\text{MnO}_3$. *Solid State Commun.* **1999**, *109*, 537–542. [[CrossRef](#)]
25. Oumezzine, M.; Hcini, S.; Baazaoui, M.; Sales, H.B.; Santos, I.M.G.d.; Oumezzine, M. Crystallite size effect on the structural, microstructure, magnetic and electrical transport properties of $\text{Pr}_{0.7}\text{Sr}_{0.3}\text{Mn}_{0.9}\text{Cr}_{0.1}\text{O}_3$ nanocrystalline via a modified Pechini method. *J. Alloys Compd.* **2013**, *571*, 79–84. [[CrossRef](#)]
26. Oumezzine, M.; Peña, O.; Guizouarn, T.; Lebullenger, R.; Oumezzine, M. Impact of the sintering temperature on the structural, magnetic and electrical transport properties of doped $\text{La}_{0.67}\text{Ba}_{0.33}\text{Mn}_{0.9}\text{Cr}_{0.1}\text{O}_3$ manganite. *J. Magn. Magn. Mater.* **2012**, *324*, 2821–2828. [[CrossRef](#)]
27. Venkataiah, G.; Reddy, P.V. Electrical behavior of sol–gel prepared $\text{Nd}_{0.67}\text{Sr}_{0.33}\text{MnO}_3$ manganite system. *J. Magn. Magn. Mater.* **2005**, *285*, 343–352. [[CrossRef](#)]
28. M'nassri, R.; Boudjada, C.; Cheikhrouhou, A. Impact of sintering temperature on the magnetic and magnetocaloric properties in $\text{Pr}_{0.5}\text{Eu}_{0.1}\text{Sr}_{0.4}\text{MnO}_3$ manganites. *J. Alloys Compd.* **2015**, *626*, 20–28. [[CrossRef](#)]
29. Moualhi, Y.; M'nassri, R.; Nofal, M.M.; Rahmouni, H.; Selmi, A.; Gassoumi, M.; Chniba-Boudjada, N.; Khirouni, K.; Cheikhrouhou, A. Influence of Fe doping on physical properties of charge ordered praseodymium–calcium–manganite material. *Eur. Phys. J. Plus* **2020**, *135*, 809. [[CrossRef](#)]
30. Rahmouni, H.; Nouiri, M.; Jemai, R.; Kallel, N.; Rzigua, F.; Selmi, A.; Khirouni, K.; Alaya, S. Electrical conductivity and complex impedance analysis of 20% Ti-doped $\text{La}_{0.7}\text{Sr}_{0.3}\text{MnO}_3$ perovskite. *J. Magn. Magn. Mater.* **2007**, *316*, 23–28. [[CrossRef](#)]
31. Rahmouni, H.; Jemai, R.; Nouiri, M.; Kallel, N.; Rzigua, F.; Selmi, A.; Khirouni, K.; Alaya, S. Admittance spectroscopy and complex impedance analysis of Ti-modified $\text{La}_{0.7}\text{Sr}_{0.3}\text{MnO}_3$. *J. Cryst. Growth* **2008**, *310*, 556–561. [[CrossRef](#)]
32. Rahmouni, H.; Selmi, A.; Khirouni, K.; Kallel, N. Chromium effects on the transport properties in $\text{La}_{0.7}\text{Sr}_{0.3}\text{Mn}_{1-x}\text{Cr}_x\text{O}_3$. *J. Alloys Compd.* **2012**, *533*, 93–96. [[CrossRef](#)]
33. Kumar, V.P.; Dayal, V.; Hadimani, R.L.; Bhowmik, R.N.; Jiles, D.C. Magnetic and electrical properties of Ti-substituted lanthanum bismuth manganites. *J. Mater. Sci.* **2015**, *50*, 3562–3575. [[CrossRef](#)]
34. Khan, A.A.; Fayaz, M.U.; Khan, M.N.; Iqbal, M.; Majeed, A.; Bilkees, R.; Mukhtar, S.; Javed, M. Investigation of charge transport mechanism in semiconducting $\text{La}_{0.5}\text{Ca}_{0.5}\text{Mn}_{0.5}\text{Fe}_{0.5}\text{O}_3$ manganite prepared by sol–gel method. *J. Mater. Sci. Mater. Electron.* **2018**, *29*, 13577–13587. [[CrossRef](#)]

35. Sacanell, J.; Sánchez, J.H.; López, A.E.R.; Martinelli, H.; Siepe, J.; Leyva, A.G.; Ferrari, V.; Juan, D.; Pruneda, M.; Gómez, A.M.; et al. Oxygen Reduction Mechanisms in Nanostructured $\text{La}_{0.8}\text{Sr}_{0.2}\text{MnO}_3$ Cathodes for Solid Oxide Fuel Cells. *J. Phys. Chem.* **2017**, *121*, 6533–6539. [[CrossRef](#)]
36. Carthy, B.P.M.; Pederson, L.R.; Chou, Y.S.; Zhou, X.; Surdoval, W.A.; Wilson, L.C. Low-temperature sintering of lanthanum strontium manganite-based contact pastes for SOFCs. *J. Power Sources* **2008**, *180*, 294–300.
37. Wu, J.; Yan, D.; Pu, J.; Chi, B.; Jian, L. The investigation of interaction between $\text{La}_{0.9}\text{Sr}_{0.1}\text{MnO}_3$ cathode and metallic interconnect for solid oxide fuel cell at reduced temperature. *J. Power Sources* **2012**, *202*, 166–174. [[CrossRef](#)]
38. Uskoković, V.; Košak, A.; Drofenik, M. Silica-coated lanthanum–strontium manganites for hyperthermia treatments. *Mater. Lett.* **2006**, *60*, 2620–2622. [[CrossRef](#)]
39. Manh, D.H.; Phong, P.T.; Namb, P.H.; Tung, D.K.; Phuc, N.X.; Lee, I.J. Structural and magnetic study of $\text{La}_{0.7}\text{Sr}_{0.3}\text{MnO}_3$ nanoparticles and AC magnetic heating characteristics for hyperthermia applications. *Phys. B* **2014**, *444*, 94–102. [[CrossRef](#)]
40. Ju, J.; Lin, J.; Wang, Y.; Zhang, Y.; Xia, C. Electrical performance of nanostructured strontium-doped lanthanum manganite impregnated onto yttria-stabilized zirconia backbone. *J. Power Sources* **2016**, *302*, 298–307. [[CrossRef](#)]
41. Qiu, J.; Jin, K.; Han, P.; Lu, H.; Hu, C.; Wang, B.; Yang, G. A theoretical study on the transport property of the $\text{La}_{0.7}\text{Sr}_{0.3}\text{MnO}_3/\text{Si}$ p-n heterojunction. *Europhys. Lett.* **2007**, *79*, 57004. [[CrossRef](#)]
42. Hu, C.-L.; Jin, K.-J.; Han, P.; Lu, H.-B.; Liao, L.; Yang, G.-Z. Theoretical study on the positive magnetoresistance in perovskite oxide p–n junctions. *Solid State Commun.* **2009**, *149*, 334–336. [[CrossRef](#)]
43. Rahmouni, H.; Jemai, R.; Kallel, N.; Selmi, A.; Khirouni, K. Titanium effects on the transport properties in $\text{La}_{0.7}\text{Sr}_{0.3}\text{Mn}_{1-x}\text{Ti}_x\text{O}_3$. *J. Alloys Compd.* **2010**, *497*, 1–5. [[CrossRef](#)]
44. Venkataiah, G.; Prasad, V.; Reddy, P.V. Structure and electrical transport of some Cd-doped $\text{La}_{0.67}\text{Sr}_{0.33}\text{MnO}_3$ manganites. *Phys. Status Solidi* **2006**, *203*, 2478–2487. [[CrossRef](#)]
45. Choi, J.H.; Jang, J.H.; Ryu, J.H.; Oh, S.M. Microstructure and cathodic performance of $\text{La}_{0.9}\text{Sr}_{0.1}\text{MnO}_3$ electrodes according to particle size of starting powder. *J. Power Sources* **2000**, *87*, 92–100. [[CrossRef](#)]
46. Shinde, K.P.; Thorat, N.D.; Pawar, S.S.; Pawar, S.H. Combustion synthesis and characterization of perovskite $\text{La}_{0.9}\text{Sr}_{0.1}\text{MnO}_3$. *Mater. Chem. Phys.* **2012**, *134*, 881–885. [[CrossRef](#)]
47. Korolyov, A.V.; Arkhipov, V.Y.; Gaviko, V.S.; Mukovskii, Y.; Arsenov, A.A.; Lapina, T.P.; Bader, S.D.; Jiang, J.S.; Nizhankovskii, V.I. Magnetic properties and magnetic states in $\text{La}_{0.9}\text{Sr}_{0.1}\text{MnO}_3$. *J. Magn. Magn. Mater.* **2000**, *213*, 63–74. [[CrossRef](#)]
48. Arkhipov, V.E.; Gaviko, V.S.; Korolyov, A.V.; Naish, V.E.; Marchenkov, V.V.; Mukovskii, Y.M.; Karabashev, S.G.; Shulyatev, D.A.; Arsenov, A.A. Structural and magnetic phase transition in $\text{La}_{0.9}\text{Sr}_{0.1}\text{MnO}_3$. *J. Magn. Magn. Mater.* **1999**, *196*, 539–540. [[CrossRef](#)]
49. Shinde, K.P.; Pawar, S.S.; Pawar, S.H. Influence of annealing temperature on morphological and magnetic properties of $\text{La}_{0.9}\text{Sr}_{0.1}\text{MnO}_3$. *Appl. Surf. Sci.* **2011**, *257*, 9996–9999. [[CrossRef](#)]
50. Das, S.; Chowdhury, P.; Rao, T.K.G.; Das, D.; Bahadur, D. Influence of grain size and grain boundaries on the properties of $\text{La}_{0.7}\text{Sr}_{0.3}\text{Co}_x\text{Mn}_{1-x}\text{O}_3$. *Solid State Commun.* **2002**, *121*, 691–695. [[CrossRef](#)]
51. Hizi, W.; Rahmouni, H.; Gassoumi, M.; Khirouni, K.; Dhahri, S. Transport properties of $\text{La}_{0.9}\text{Sr}_{0.1}\text{MnO}_3$ manganite. *Eur. Phys. J. Plus* **2020**, *135*, 456. [[CrossRef](#)]
52. Choudhary, Y.R.S.; Mangavati, S.; Patil, S.; Rao, A.; Nagaraja, B.S.; Thomas, R.; Kini, S.G. Effect of rare-earth substitution at La-site on structural, electrical and thermoelectric properties of $\text{La}_{0.7-x}\text{RE}_x\text{Sr}_{0.3}\text{MnO}_3$ compounds ($x = 0, 0.2, 0.3$; RE = Eu, Gd, Y). *J. Magn. Magn. Mater.* **2018**, *451*, 110–120. [[CrossRef](#)]
53. Chen, G.J.; Chang, Y.H.; Hsu, H.W. The effect of microstructure and secondary phase on magnetic and electrical properties of La-deficient $\text{La}_{1-x}\text{MnO}_{3-\delta}$ ($0 \leq x \leq 0.3$) films. *J. Magn. Magn. Mater.* **2000**, *219*, 317–324. [[CrossRef](#)]
54. Yousefi, S.; Trappen, R.; Mottaghi, N.; Bristow, A.D.; Holcomb, M.B. Oxygen vacancy effect on ultra-fast carrier dynamics of perovskite oxide $\text{La}_{0.7}\text{Sr}_{0.3}\text{MnO}_3$ thin films, Ultrafast Phenomena and Nanophotonics XXIV. *Int. Soc. Opt. Photonics* **2020**, *11278*, 112780.
55. Dhahri, R.; Bejar, M.; Hajlaoui, M.; Sdiri, N.; Valente, M.A.; Dhahri, E. Structural properties and electrical behaviour in the polycrystalline lanthanum-deficiency $\text{La}_{1-x}\text{MnO}_3$ manganites. *J. Magn. Magn. Mater.* **2009**, *321*, 1735–1738. [[CrossRef](#)]
56. Ji, D.H.; Tang, G.D.; Li, Z.Z.; Han, Q.J.; Hou, X.; Bian, R.R.; Liu, S.R. Investigation on the maximum content of vacancy at the B sites in $\text{La}_{0.75}\text{Sr}_{0.25}\text{Mn}_{1-x}\text{O}_3$ perovskite manganites. *J. Appl. Phys.* **2012**, *111*, 113902. [[CrossRef](#)]
57. Abdelmoula, N.; Guidara, K.; Cheikh-Rouhou, A.; Dhahri, E. Effects of the Oxygen Nonstoichiometry on the Physical Properties of $\text{La}_{0.7}\text{Sr}_{0.3}\text{MnO}_{3-\delta}$ Manganites ($0 \leq \delta \leq 0.15$). *J. Solid State Chem.* **2000**, *151*, 139–144. [[CrossRef](#)]
58. Malavasi, L.; Mozzati, M.C.; Azzoni, C.B.; Chiodelli, G.; Flor, G. Role of oxygen content on the transport and magnetic properties of $\text{La}_{1-x}\text{Ca}_x\text{MnO}_{3+\delta}$ manganites. *Solid State Commun.* **2002**, *123*, 321–326. [[CrossRef](#)]
59. Li, Y.; Zhang, H.; Liu, X.; Chen, Q.; Chen, Q. Electrical and magnetic properties of $\text{La}_{1-x}\text{Sr}_x\text{MnO}_3$ ($0.1 \leq x \leq 0.25$) ceramics prepared by sol–gel technique. *Ceram. Int.* **2019**, *45*, 16323–16330. [[CrossRef](#)]
60. Anane, A.; Dupas, C.; le Dang, K.; Renard, J.P.; Veillet, P.; Guevara, A.M.d.; Millot, F.; Pinsardi, L.; Revcolevschi, A. Transport properties and magnetic behaviour of $\text{La}_{1-x}\text{Sr}_x\text{MnO}_3$ single crystals. *J. Phys. Condens. Matter* **1995**, *7*, 7015–7021. [[CrossRef](#)]
61. Baaziz, H.; Maaloul, N.K.; Tozri, A.; Rahmouni, H.; Mizouri, S.; Khirouni, K.; Dhahri, E. Effect of sintering temperature and grain size on the electrical transport properties of $\text{La}_{0.67}\text{Sr}_{0.33}\text{MnO}_3$ manganite. *Chem. Phys. Lett.* **2015**, *640*, 77–81. [[CrossRef](#)]

62. Mleiki, A.; Khlifi, A.; Rahmouni, H.; Guerhazi, N.; Khirouni, K.; Hlil, E.K.; Cheikhrouhou, A. Magnetic and dielectric properties of Ba-lacunar $\text{La}_{0.5}\text{Eu}_{0.2}\text{Ba}_{0.3}\text{MnO}_3$ manganites synthesized using sol-gel method under different sintering temperatures. *J. Magn. Magn. Mater.* **2020**, *502*, 166571. [[CrossRef](#)]
63. Venkataiah, G.; Krishna, D.C.; Vithal, M.; Rao, S.S.; Bhat, S.V.; Prasad, V.; Subramanyam, S.V.; Reddy, P.V. Effect of sintering temperature on electrical transport properties of $\text{La}_{0.67}\text{Ca}_{0.33}\text{MnO}_3$. *Phys. B* **2005**, *357*, 370–379. [[CrossRef](#)]
64. Venkataiah, G.; Lakshmi, Y.K.; Reddy, P.V. Influence of sintering temperature on resistivity, magnetoresistance and thermopower of $\text{La}_{0.67}\text{Ca}_{0.33}\text{MnO}_3$. *PMC Phys. B* **2008**, *1*, 7. [[CrossRef](#)]
65. Pan, K.Y.; Halim, S.A.; Lim, K.P.; Daud, W.M.; Chen, S.K. Effect of Sintering Temperature on Microstructure, Electrical and Magnetic Properties of $\text{La}_{0.85}\text{K}_{0.15}\text{MnO}_3$ Prepared by Sol-Gel Method. *J. Supercond. Nov. Magn.* **2012**, *25*, 1177–1183. [[CrossRef](#)]
66. Lakshmi, Y.K.; Reddy, P.V. Influence of sintering temperature and oxygen stoichiometry on electrical transport properties of $\text{La}_{0.67}\text{Na}_{0.33}\text{MnO}_3$ manganite. *J. Alloys Compd.* **2009**, *470*, 67–74. [[CrossRef](#)]
67. Shannigrahi, S.R.; Tan, S.Y. Effects of processing parameters on the properties of lanthanum manganite. *Mater. Chem. Phys.* **2011**, *129*, 15–18. [[CrossRef](#)]
68. Li, N.; Mahapatra, M.K.; Singh, P. Sintering of porous strontium doped lanthanum manganite-yttria stabilized zirconia composite in controlled oxygen atmosphere at 1400 °C. *J. Power Sources* **2013**, *221*, 57–63. [[CrossRef](#)]
69. Othmani, S.; Bejar, M.; Dhahri, E.; Hlil, E.K. The effect of the annealing temperature on the structural and magnetic properties of the manganites compounds. *J. Alloys Compd.* **2009**, *475*, 46–50. [[CrossRef](#)]
70. Li, C.-X.; Yang, B.; Zhang, S.-T.; Zhang, R.; Cao, W.W. Effects of sintering temperature and poling conditions on the electrical properties of $\text{Ba}_{0.70}\text{Ca}_{0.30}\text{TiO}_3$ diphasic piezoelectric ceramics. *Ceram. Int.* **2013**, *39*, 2967–2973. [[CrossRef](#)]
71. Worledge, D.C.; Snyder, G.J.; Beasley, M.R.; Geballe, T.H.; Hiskes, R.; DiCarolis, S. Anneal-tunable Curie temperature and transport of $\text{La}_{0.67}\text{Ca}_{0.33}\text{MnO}_3$. *J. Appl. Phys.* **1996**, *80*, 5158–5161. [[CrossRef](#)]
72. Dey, P.; Nath, T.K. Effect of grain size modulation on the magneto- and electronic-transport properties of $\text{La}_{0.7}\text{Ca}_{0.3}\text{MnO}_3$ nanoparticles: The role of spin-polarized tunneling at the enhanced grain surface. *Phys. Rev. B* **2006**, *73*, 214425. [[CrossRef](#)]
73. Paredes-Navia, S.A.; Liang, L.; Romo-De-La-Cruz, C.O.; Gemmen, E.; Fernandes, A.; Prucz, J.; Chen, Y.; Song, X. Electrical conductivity increase by order of magnitude through controlling sintering to tune hierarchical structure of oxide ceramics. *J. Solid State Chem.* **2021**, *294*, 121831. [[CrossRef](#)]
74. Baaziz, H.; Tozri, A.; Dhahri, E.; Hlil, E.K. Size-induced Griffiths phase-like in ferromagnetic metallic $\text{La}_{0.67}\text{Sr}_{0.33}\text{MnO}_3$ nanoparticles. *J. Magn. Magn. Mater.* **2016**, *403*, 181–187. [[CrossRef](#)]
75. Baaziz, H.; Tozri, A.; Dhahri, E.; Hlil, E.K. Influence of grain size and sintering temperature grain size on the critical behavior near the paramagnetic to ferromagnetic phase transition temperature in $\text{La}_{0.67}\text{Sr}_{0.33}\text{MnO}_3$ nanoparticles. *J. Magn. Magn. Mater.* **2018**, *449*, 207–213. [[CrossRef](#)]
76. Baaziz, H.; Tozri, A.; Dhahri, E.; Hlil, E.K. Magnetocaloric properties of $\text{La}_{0.67}\text{Sr}_{0.33}\text{MnO}_3$ tunable by particle size and dimensionality. *Chem. Phys. Lett.* **2018**, *691*, 355–359. [[CrossRef](#)]
77. Baaziz, H.; Tozri, A.; Dhahri, E.; Hlil, E.K. Effect of particle size reduction on the structural, magnetic properties and the spin excitations in ferromagnetic insulator $\text{La}_{0.9}\text{Sr}_{0.1}\text{MnO}_3$ nanoparticles. *Ceram. Int.* **2015**, *41*, 2955–2962. [[CrossRef](#)]
78. Baaziz, H.; Tozri, A.; Dhahri, E.; Hlil, E.K. Size reduction effect on the critical behavior near the paramagnetic to ferromagnetic phase transition temperature in $\text{La}_{0.9}\text{Sr}_{0.1}\text{MnO}_3$ nanoparticles. *Solid State Commun.* **2015**, *208*, 45–52. [[CrossRef](#)]
79. Baaziz, H.; Tozri, A.; Dhahri, E.; Hlil, E.K. Effect of particle size reduction on the magnetic phase transition and the magnetocaloric properties in ferromagnetic insulator $\text{La}_{0.9}\text{Sr}_{0.1}\text{MnO}_3$ nanoparticles. *Chem. Phys. Lett.* **2015**, *625*, 168–173. [[CrossRef](#)]
80. Moualhi, Y.; Rahmouni, H.; Khirouni, K. Usefulness of theoretical approaches and experiential conductivity measurements for understanding manganite-transport mechanisms. *Results Phys.* **2020**, *19*, 103570. [[CrossRef](#)]
81. Moualhi, Y.; Rahmouni, H.; Gassoumi, M.; Khirouni, K. Summerfield scaling model and conduction processes defining the transport properties of silver substituted half doped (La–Ca) MnO_3 ceramic. *Ceram. Int.* **2020**, *46*, 24710–24717. [[CrossRef](#)]
82. Banerjee, A.; Pal, S.; Bhattecharya, S.; Chaudhuri, B.K.; Yang, H.D. Particle size and magnetic field dependent resistivity and thermoelectric power of $\text{La}_{0.5}\text{Pb}_{0.5}\text{MnO}_3$ above and below metal–insulator transition. *J. Appl. Phys.* **2002**, *91*, 5125–5134. [[CrossRef](#)]
83. Venkataiah, G.; Lakshmi, Y.K.; Prasad, V.; Reddy, P.V. Influence of Particle Size on Electrical Transport Properties of $\text{La}_{0.67}\text{Sr}_{0.33}\text{MnO}_3$ Manganite System. *J. Nanosci. Nanotechnol.* **2007**, *7*, 2000–2004. [[CrossRef](#)] [[PubMed](#)]
84. Huang, Y.-H.; Yan, C.-H.; Wang, Z.-M.; Liao, C.-S.; Xu, G.-X. Variation of structural, magnetic and transport properties in $\text{RE}_{0.7}\text{Sr}_{0.3}\text{MnO}_3$ granular perovskites. *Solid State Commun.* **2001**, *118*, 541–546. [[CrossRef](#)]
85. Venkataiah, G.; Huang, J.C.A.; Reddy, P.V. Low temperature resistivity minimum and its correlation with magnetoresistance in $\text{La}_{0.67}\text{Ba}_{0.33}\text{MnO}_3$ nanomanganites. *J. Magn. Magn. Mater.* **2010**, *322*, 417–423. [[CrossRef](#)]
86. Mleiki, A.; Hanen, R.; Rahmouni, H.; Guerhazi, N.; Khirouni, K.; Hli, E.K.; Cheikhrouhou, A. Study of magnetic and electrical properties of $\text{Pr}_{0.65}\text{Ca}_{0.25}\text{Ba}_{0.1}\text{MnO}_3$ manganite. *RSC Adv.* **2018**, *8*, 31755–31763. [[CrossRef](#)]
87. Hanen, R.; Mleiki, A.; Rahmouni, H.; Guerhazi, N.; Khirouni, K.; Hlil, E.K.; Cheikhrouhou, A. Effect of the nature of the dopant element on the physical properties of X-PrCaMnO system (X = Cd, Sr, and Pb). *J. Magn. Magn. Mater.* **2020**, *508*, 166810. [[CrossRef](#)]
88. Hayat, K.; Nadeem, M.; Iqbal, M.J.; Rafiq, M.A.; Hasan, M.M. Analysis of electro-active regions and conductivity of BaMnO_3 ceramic by impedance spectroscopy. *Appl. Phys. A* **2014**, *115*, 1281–1289. [[CrossRef](#)]

89. Li, M.; Sinclair, D.C. The extrinsic origins of high permittivity and its temperature and frequency dependence in $Y_{0.5}Ca_{0.5}MnO_3$ and $La_{1.5}Sr_{0.5}NiO_4$ ceramics. *J. Appl. Phys.* **2012**, *111*, 054106. [[CrossRef](#)]
90. Moualhi, Y.; Nofal, M.M.; M'nassri, R.; Rahmouni, H.; Selmi, A.; Gassoumi, M.; Khirouni, K.; Cheikhrouhou, A. Double Jonscher response and contribution of multiple mechanisms in electrical conductivity processes of Fe-PrCaMnO ceramic. *Ceram. Int.* **2020**, *46*, 1601–1608. [[CrossRef](#)]
91. Moualhi, Y.; M'nassri, R.; Nofal, M.M.; Rahmouni, H.; Selmi, A.; Gassoumi, M.; Chniba-Boudjada, N.; Khirouni, K.; Cheikhrouhou, A. Magnetic properties and impedance spectroscopic analysis in $Pr_{0.7}Ca_{0.3}Mn_{0.95}Fe_{0.05}O_3$ perovskite ceramic. *J. Mater. Sci. Mater. Electron.* **2020**, *31*, 21046–21058. [[CrossRef](#)]
92. Lahouli, R.; Massoudi, J.; Smari, M.; Rahmouni, H.; Khirouni, K.; Dhahri, E.; Bessais, L. Investigation of annealing effects on the physical properties of $Ni_{0.6}Zn_{0.4}Fe_{1.5}Al_{0.5}O_4$ ferrite. *RSC Adv.* **2019**, *9*, 19949–19964. [[CrossRef](#)]